Resistive Wall Mode Control Code Maturity

Yueqiang Liu[1], M.S. Chu[2], W.F. Guo[3], F. Villone[4], R. Albanese[5], G. Ambrosino[4], M. Baruzzo[6], T. Bolzonella[6], I.T. Chapman[1], A.M. Garofalo[2], C.G. Gimblett[1], R.J. Hastie[1], T.C. Hender[1], G.L. Jackson[2], R.J. La Haye[2], M.J. Lanctot[7], Y.K. In[8], G. Machiori[6], M. Okabayashi[9], R. Paccagnella[6], M. Furno Palumbo[4], A. Pironti[4], H. Reimerdes[7], G. Rubinacci[5], A. Soppelsa[6], E.J. Strait[2], S. Ventre[4], D. Yadykin[10]

[1]Euratom/CCFE Fusion Association, Culham Science Centre, Abingdon, OX14 3DB, UK

[2] General Atomics, San Diego, California, 92186-5608, USA

[3] ASIPP Institute of Plasma Physics, Chinese Academy of Sciences, Hefei 230031, China

[4] ENEA/CREATE, DAEIMI, Universita di Cassino, Via di Biasio 43, Cassino (FR), Italy

[5] ENEA/CREATE, Universita Federico II di Napoli, Via Claudio 21, Napoli, Italy

[6] Consorzio RFX, Corso Stati Uniti 4, Padova, 35127, Italy

[7] Columbia University, 2960 Broadway, New York, New York, 10027-6902, USA

[8] FAR-TECH, Inc., 3550 General Atomics Court, San Diego, California, USA

[9] Princeton Plasma Physics Laboratory, Princeton, New Jersey, 08543-0451, USA

[10] Eurantom/VR Fusion Association, Chalmers University of Technology, Gotheburg, S-41296, Sweden

E-mail: `yueqiang.liu@ccfe.ac.uk`

Abstract. Two issues of the resistive wall mode (RWM) control code maturity are addressed: the inclusion of advanced mode damping physics beyond the ideal MHD description, and the possibility of taking into account the influence of 3D features of the conducting structures on the mode stability and control. Examples of formulations and computational results are given, using the MARS-F/K codes and the CarMa code.

PACS numbers: 52.35.Py, 28.52.Av, 52.55.Fa, 52.65.Kj

Submitted to: *Plasma Phys. Control. Fusion*

1. Introduction

The resistive wall mode (RWM) is normally understood as an ideal external kink mode that is unstable. But the presence of conducting structures (resistive walls) surrounding the plasma reduces significantly the growth rate of the mode, typically down to the inverse wall time. For long pulse or steady state operation of fusion devices, the RWM instability can pose a severe limitation on the operational space, especially in terms of the achievable plasma pressure. This mode is one of the particular concerns for ITER steady state scenarios [1].

The physics and control of the RWM have been extensively investigated in the last 10-20 years, both in theory and experiments [2]. Significant modelling efforts have been devoted to understanding the present experimental results, and to predicting the RWM behaviour in future devices such as ITER. Driven by the needs of quantitative interpretation of new experimental observations, realistic modelling of the experimental geometry, and reliable prediction for ITER plasmas, the RWM codes have become more mature in the modelling capability of both the physics and the geometry.

Several RWM control codes have been developed during the last 5-10 years, each with one or another advanced features, compared to the standard ideal MHD computation of the ideal kink instability for a static plasma. We start a short survey of the commonly used codes by clarifying some terminology first. The word "control" is understood here in a generic sense, that includes both passive and active control of the RWM. The passive control refers to the mode stabilisation by plasma rotation or other physics-based damping mechanisms. The active control refers to the feedback stabilisation of the mode using active magnetic coils. The word "maturity" reflects specifically the capability of present RWM codes in modelling the realistic experimental situations.

A cluster of codes are focused on studying the advanced MHD-kinetic physics associated with the RWM. The most advanced among them are the AEGIS-K code [3] and the LIGKA code [4]. Both are based on the linear gyro-kinetic formulation. There are several MHD-kinetic hybrid codes, such as MISK [5], MISHKA+HAGIS [6] and MARS-K [7]. These codes include the drift-kinetic effects into MHD equations by considering the kinetic resonances between the particle (thermal or fast) drift motions (bounce or toroidal precession) and the RWM. The MISHKA+HAGIS code takes into account the full particle drift orbit (the finite banana width for trapped particles) effects, whilst the MISK and MARS-K codes so far assume a vanishing drift orbit width. The MISK and MISHKA+HAGIS codes follow a perturbative MHD-kinetic hybrid approach, in which the perturbed kinetic energy is computed using the fluid eigenfunction of a marginally stable ideal kink mode. The MARS-K code follows a self-consistent approach, in which the RWM eigenfunction is allowed to be modified by the kinetic effects.

Another cluster of RWM codes tries to model as realistic as possible the conducting structures outside the plasma. Since the stability of the RWM is strongly affected by the surrounding conducting walls (most of the free MHD potential energy of an

ideal external kink mode is dissipated through the wall eddy current), the 3D features, such as the holes, the gaps in the wall, can significantly modify the wall eddy current pattern and hence the growth rate of the mode. The above mentioned RWM codes with advanced kinetic physics either do not include resistive walls, or use a complete, thin shell approximation for the walls (2D walls). The codes VALEN [8], STARWALL [9, 10] and CarMa [11, 12] are capable of modelling 3D walls. VALEN and STARWALL use the thin shell approximations for the wall (surface current patches). CarMa can include volumetric eddy currents. All these three codes are based on the ideal MHD, mass-free description for the plasma. No plasma inertia, rotation, kinetic effects are included. The feedback option is included in all three codes.

There are also codes that have a 2D wall approximation but that do include the feedback option, such as the MARS-F code [13], NMA code [14, 15] and the KINX code [16].

A new implementation of the CarMa code [17] includes both 3D wall effects and the advanced kinetic damping physics for the RWM modelling. Active control of the RWM can also be studied using this code.

This paper will describe the MARS-F/K and the CarMa codes, as examples to illustrate the key issues and solutions for the RWM control codes. The next Section gives a brief introduction to the mathematical formulations behind these codes. Section 3 reports some of the recent code modelling results. These examples are chosen to show the current status of the RWM control code maturity.

2. Formulations behind advanced RWM control codes

The detailed formulations behind the MARS-F/K and the CarMa codes have been documented in various publications. Below we make a short, but complete summary of the key elements in these formulations. The portion related to the fast ions is new, and will be described in more detail.

2.1. Formulations behind MARS-F/K

MARS-F is a single fluid, full MHD eigenvalue code in full toroidal geometry. It solves the MHD equations with toroidal flow, and with several extensions

- a pure vacuum region surrounding the plasma
- a set of radially separated, toroidally complete resistive walls in the vacuum region. The wall shape can follow the shape of the conducting vacuum vessels in experiments (normally non-conformal to the plasma boundary). The wall thickness is assumed to be much smaller than the plasma minor radius, and much smaller than the skin depth of the wall eddy currents induced by the plasma instability or external sources (so-called thin-wall approximation).
- a set of magnetic coils located in the vacuum region. The number and the location of the coils along the poloidal angle can be arbitrary. The number of coils along

the toroidal angle ϕ is assumed sufficiently large in order to represent the $\exp(in\phi)$-distribution of the coil current, for a single, given toroidal mode number n.

Separate equations are associated with each of the above extensions. These equations are solved together with the perturbed MHD equations inside the plasma.

The MARS-K code is based on MARS-F, by adding the drift-kinetic effects into the plasma, forming a MHD-kinetic hybrid code. The full set of equations inside the plasma read

$$(\gamma + in\Omega)\xi = \mathbf{v} + (\xi \cdot \nabla\Omega)R\hat{\phi}, \tag{1}$$

$$\rho(\gamma + in\Omega)\mathbf{v} = -\nabla \cdot \mathbf{p} + \mathbf{j} \times \mathbf{B} + \mathbf{J} \times \mathbf{Q} - \rho\left[2\Omega\hat{\mathbf{Z}} \times \mathbf{v} + (\mathbf{v} \cdot \nabla\Omega)R\hat{\phi}\right], \tag{2}$$

$$(\gamma + in\Omega)\mathbf{Q} = \nabla \times (\mathbf{v} \times \mathbf{B}) + (\mathbf{Q} \cdot \nabla\Omega)R\hat{\phi}, \tag{3}$$

$$(\gamma + in\Omega)p = -\mathbf{v} \cdot \nabla P, \tag{4}$$

$$\mathbf{j} = \nabla \times \mathbf{Q}, \tag{5}$$

$$\mathbf{p} = p\mathbf{I} + p_{\parallel}\hat{\mathbf{b}}\hat{\mathbf{b}} + p_{\perp}(\mathbf{I} - \hat{\mathbf{b}}\hat{\mathbf{b}}), \tag{6}$$

where $\mathbf{B}, \mathbf{J}, \mathbf{P}$ are equilibrium magnetic field, current, and pressure respectively. Ω is the plasma fluid rotation frequency along the toroidal angle ϕ. This is normally due to the $E \times B$ rotation. We use a static equilibrium even in the presence of flow, which is valid if the flow speed is much smaller than the sound speed. [The equilibrium correction due to the toroidal flow is the order of the sound Mach number squared.]

The variables $\xi, \mathbf{v}, \mathbf{Q}, \mathbf{j}, \mathbf{p}$ represent the plasma displacement, perturbed velocity, magnetic field, current, and pressure tensor, respectively. ρ is the unperturbed plasma density. γ is the eigenvalue that we are looking for. R is the plasma major radius, $\hat{\mathbf{Z}}$ the unit vector in the vertical direction, $\mathbf{I}$ the unit tensor.

The drift kinetic terms enter into the MHD equations via the perturbed kinetic pressure tensors shown in Eq. (6), where p is the scalar fluid pressure perturbation, and $p_{||}(\xi_{\perp}), p_{\perp}(\xi_{\perp})$ are the parallel and perpendicular components of the kinetic pressure perturbations, respectively. $\hat{\mathbf{b}} = \mathbf{B}/|\mathbf{B}|$ is the unit vector for the equilibrium magnetic field. The drift kinetic pressure tensors, which are functions of the plasma displacement $\xi_{\perp}$ perpendicular to the equilibrium magnetic field line, are included into MHD via the momentum equation (2). This allows a self-consistent modification of the eigenfunctions due to the kinetic effects.

The perturbed kinetic pressures are computed via

$$p_{\parallel}e^{-i\omega t+in\phi} = \sum_{e,i}\int d\Gamma M v_{\parallel}^2 f_1^{th} + \int d\Gamma M v_{\parallel}^2 f_1^h,$$

$$p_{\perp}e^{-i\omega t+in\phi} = \sum_{e,i}\int d\Gamma \frac{1}{2} M v_{\perp}^2 f_1^{th} + \int d\Gamma \frac{1}{2} M v_{\perp}^2 f_1^h,$$

where an $\exp(-i\omega t + in\phi)$-dependence is explicitly assumed for the perturbations, with the mode frequency $\omega \equiv i\gamma$. The integral is carried out over the particle velocity space Γ. M is the (thermal or fast) particle mass, $v_{\parallel}, v_{\perp}$ are the parallel and perpendicular (to the equilibrium magnetic field) velocity of the particle bounce motion. f_1^{th} and f_1^h are the perturbed distribution functions for thermal particles (ions and electrons) and fast ions

respectively. These functions are derived by solving the perturbed drift kinetic equations for each particle species, following the approaches by Antonsen [18] and Porcelli [19]. Details on how these derivations are adapted to the MARS-K formulation are reported in [7] for thermal particles. A similar approach is followed for fast ions.

We assume a slowing-down (Lorenzian) equilibrium distribution function for fast ions

$$f_0^h = \begin{cases} \frac{C}{\epsilon_k^{3/2}+\epsilon_c^{3/2}} & 0 < \epsilon_k < \epsilon_{\max} \\ 0 & \epsilon_k > \epsilon_{\max} \end{cases} \tag{7}$$

where

$$\epsilon_c = \left(\frac{3\sqrt{\pi}}{4}\right)^{2/3} \left(\frac{M_h}{M_i}\right) \left(\frac{M_i}{M_e}\right)^{1/3} T_e.$$

M_i, M_e and M_h are particle masses for thermal ions, electrons, and fast ions respectively. T_e is the electron temperature. $\epsilon_{\max} = 3.52$Mev for the fusion born α-particles. For beam or rf-wave generated hot ions, $\epsilon_{\max}$ is generally a function of the minor radius and is determined from the experimental measurements. The parameter C can be found by specifying the radial density distribution $N_h = \int f_0^h d\Gamma$ of the fast ions

$$C = N_h M_h^{3/2} A,$$

where

$$A \equiv \left(4\sqrt{2}\pi \int_0^1 \frac{\tilde{\epsilon}_k^{1/2} d\tilde{\epsilon}_k}{\tilde{\epsilon}_k^{3/2} + \tilde{\epsilon}_c^{3/2}}\right)^{-1} = \frac{3}{8\sqrt{2}\pi} \frac{1}{\ln(1+\tilde{\epsilon}_c^{-3/2})},$$

and $\tilde{\epsilon}_k \equiv \epsilon_k/\epsilon_{\max}, \tilde{\epsilon}_c = \epsilon_c/\epsilon_{\max}$.

We point out that the slowing-down distribution (7) is probably a reasonable approximation for the α-particles, but a crude one for the hot ions from additional heating, which are normally anisotropic in the pitch angle. This will be improved in the future work.

The equilibrium kinetic pressure due to fast ions is calculated as

$$P_h = \int f_0^h \frac{1}{3} M_h v^2 d\Gamma = \frac{8\sqrt{2}\pi}{3} A C_h N_h \epsilon_{\max}, \tag{8}$$

where

$$\begin{aligned} C_h(\epsilon_{\max}) \quad &\equiv \int_0^1 \frac{\tilde{\epsilon}_k^{3/2} d\tilde{\epsilon}_k}{\tilde{\epsilon}_k^{3/2} + \tilde{\epsilon}_c^{3/2}} \\ &= 1 - \frac{\tilde{\epsilon}_c}{9}\left[\sqrt{3}\pi - 6\sqrt{3}\mathrm{atan}\frac{-2+\sqrt{\tilde{\epsilon}_c}}{\sqrt{3\tilde{\epsilon}_c}} - 6\ln(1+\sqrt{\tilde{\epsilon}_c}) + 3\ln(1-\sqrt{\tilde{\epsilon}_c}+\tilde{\epsilon}_c)\right]. \end{aligned}$$

In practice, if the pressure profile P_h for hot ions is measured, the value of $\epsilon_{\max}$ can then be computed by solving the non-linear algebraic equation (8) with respect to $\epsilon_{\max}$, at each radial point.

The portion of the perturbed kinetic pressure, associated with the fast ions, can be derived following the similar procedure as outlined in Ref. [7]. The poloidal Fourier

harmonics (after multiplying by the Jacobian J of the chosen flux coordinate system) read

$$(Jp_h^g)_k = \frac{2\sqrt{2}\pi}{B_0} A N_h \epsilon_{\max} \sum_{m,l,u,\sigma} \int_0^1 d\tilde{\epsilon}_k \frac{\tilde{\epsilon}_k^{5/2}}{\tilde{\epsilon}_k^{3/2} + \tilde{\epsilon}_c^{3/2}} \int d\Lambda \lambda H_{ml}^u G_{kml}^g X_m^u, \tag{9}$$

where $\sigma = \text{sign}(v_\parallel)$, g stands for $\parallel$ or $\perp$. $\Lambda \equiv \mu B_0/\epsilon_k$ is the particle pitch angle, with μ being the magnetic moment and B_0 the on-axis equilibrium magnetic field amplitude. H_{ml}^u and G_{kml}^g are defined the same as in Ref. [7], but for fast ions. X_m^u represent the poloidal Fourier harmonics of the solution variables $\xi_\perp$ and $\mathbf{Q}$. For trapped fast ions, we consider only the bounce harmonic $l = 0$. λ is the resonance operator for trapped fast ions

$$\lambda = \frac{1}{n\omega_d^h + n\omega_E - \omega} \left[\frac{3\tilde{\epsilon}_k^{1/2}/2}{\tilde{\epsilon}_k^{3/2} + \tilde{\epsilon}_c^{3/2}} (n\omega_E - \omega) + \right.$$
$$\left. \frac{n\epsilon_{\max}}{e} \left(\frac{1}{\tilde{\epsilon}_k^{3/2} + \tilde{\epsilon}_c^{3/2}} \frac{d\tilde{\epsilon}_c^{3/2}}{d\psi} - \frac{1}{N_h A} \frac{d(N_h A)}{d\psi} \right) \right], \tag{10}$$

where ω_d^h is the bounce-orbit-averaged fast ion precession frequency (in the plasma frame). $\omega \equiv i\gamma$ is the (complex) eigenmode frequency.

In the self-consistent approach, the unknown eigenvalue γ enters into the resonance operator (10) for fast ions (as well as for thermal particles), leading to an eigenvalue problem that is non-linear with respect to γ. An iterative procedure is needed to find the converged eigenvalue. At each iteration, the computed coefficients before the solution variables X_m^u in (9) are added to the system matrices, together with those coefficients from the MHD operators.

In the perturbative option of MARS-K, we compute the perturbed kinetic energy due to trapped fast ions

$$\delta W_k^h = \sqrt{2}\pi^2 \int \frac{d\psi}{B_0} A N_h \epsilon_{\max} \int d\Lambda \hat{\tau}_b \int_0^1 d\tilde{\epsilon}_k \frac{\tilde{\epsilon}_k^{5/2}}{\tilde{\epsilon}_k^{3/2} + \tilde{\epsilon}_c^{3/2}} \lambda \left| \left\langle e^{in\tilde{\phi}(t)} H_L \right\rangle \right|^2,$$

where ψ is the normalised poloidal flux. $\hat{\tau}_b$ is the particle bounce period normalised by $\sqrt{M_h/2\epsilon_k}$. $< \cdot >$ denotes averaging over the particle bounce orbit. $\tilde{\phi}$ is the secular part of the particle phase along the toroidal angle as it drifts. And

$$H_L(s, \chi, \Lambda) \equiv 2 \left(1 - \Lambda \frac{B}{B_0}\right) \xi_\perp \cdot \kappa + \frac{\Lambda}{B_0} (Q_\parallel + \xi_\perp \cdot \nabla B),$$

where $B = |\mathbf{B}|$, and κ is the equilibrium field line curvature.

In the perturbative approach, we normally use the eigenfunction $(\xi_\perp, Q_\parallel)$ of the fluid RWM for evaluating H_L and δW_k^h. The eigenfrequency of the fluid RWM $\omega = i\gamma_f$ is used for computing the resonance operator λ. The eigenvalue of the kinetic RWM is then computed using the dispersion relation [20, 21]

$$\gamma \tau_w^* = -\frac{\delta W_\infty + \delta W_k}{\delta W_b + \delta W_k} \tag{11}$$

where τ_w^* is the modified wall time as defined in [20, 21]. δW_∞ is the fluid potential energy (including both the plasma and the vacuum contributions) without wall, and δW_b is the fluid potential energy with a perfectly conducting wall at the minor radius b. δW_k is the total drift kinetic potential energy due to thermal and fast particles.

2.2. Formulations behind CarMa

The CarMa code couples MARS-F/K with the 3D eddy current code CARIDDI [22]. CARIDDI solves quasi-magnetostatic Maxwell's equations in an integral formulation. This formulation is best suited to solving eddy current problems in an open domain, where the (3D) conductors occupy a relatively small volume or surface area. Numerically, a finite element method is used in CARIDDI, where the so-called edge elements [23] are utilised as the basis functions. For an electromagnetic problem where sharp variations of material properties occur, edge elements are a "natural" choice since they preserve the exact continuity conditions on the electromagnetic fields $(\mathbf{E}, \mathbf{H}, \mathbf{A})$, that are imposed by the Maxwell equations. Other types of elements, such as the nodal elements normally have difficulty in solving problems with sharp material variations, since they over-constrain the continuity of the solution. Specific techniques have to be applied, in order to relax the constraints from nodal elements.

Another key feature of the CARIDDI code is the implementation of a fast numerical technique to speed up, by orders of magnitude, the electromagnetic computations. This technique, combined with the possibility of parallel computing, allows the code to solve very large eddy current problems [24]. This will be demonstrated by examples in the next Section.

The key issue of the CarMa formulation is the coupling strategy between the eddy current code and the MHD code. Two coupling schemes have been proposed and successfully tested.

The so-called "forward" coupling scheme has been documented in detail in our previous publications [11, 12, 25]. The key idea is to introduce an arbitrary coupling surface just outside the plasma surface, and to replace the magnetic response of the plasma to the external world by the response of the virtual surface currents in the coupling surface. This can be rigorously shown to be possible for an arbitrary toroidal system [26]. Effectively, the forward coupling scheme "embeds" the MHD equations into the eddy current formulation. Based on this scheme, CarMa has been used to study the RWM stability and control in several devices [27, 28, 29, 30] including ITER.

The forward coupling strategy has been very successful for the RWM modelling, provided the so-called inertia-free approximation is valid for the mode. Since the stability of a RWM is normally determined by the wall eddy current, the plasma mass plays a minor role (unlike the ideal kink modes). The plasma inertia effect can normally be neglected for the RWM. In this case, what we need is just to compute the *static* response of the plasma. However, there are cases when the plasma inertia cannot be neglected. For instance, when the plasma is close to the ideal-wall beta limit, or when the plasma flow effects are important. Adding the drift kinetic effects into the MHD equations complicates further the matter. It is not impossible, but difficult to overcome this problem by considering the *dynamic* response of the plasma, since the RWM dynamics can have rather high degrees of freedom.

A more elegant way to solve the problem is the "backward" coupling strategy

[25, 17]. Here we "embed" the *dynamic* response of the conducting structures into the MHD-kinetic equations. Again we introduce a coupling surface just outside the plasma boundary surface. It has been shown that the dynamic response of the conductors, to the magnetic field perturbations from the plasma, can be formulated as a linear relation with respect to the eigenvalue γ [25, 31, 32]. In CarMa formulation, we derive a vector expression that relates the normal component $\mathbf{b}_N$ to the tangential (either poloidal or toroidal) component $\mathbf{b}_T$ of the *total* perturbed magnetic field at the coupling surface

$$\left(\overleftrightarrow{\mathbf{A}}_{0N} + \gamma\overleftrightarrow{\mathbf{A}}_{1N}\right)\mathbf{b}_N + \left(\overleftrightarrow{\mathbf{A}}_{0T} + \gamma\overleftrightarrow{\mathbf{A}}_{1T}\right)\mathbf{b}_T = 0, \tag{12}$$

where all the coefficient matrices $\overleftrightarrow{\mathbf{A}}_{0N}, \overleftrightarrow{\mathbf{A}}_{1N}, \cdots$ are constant matrices (i.e. do not depend on γ). Essentially these matrices contain all the mutual couplings between the conductor eddy currents, the perturbed plasma currents and the perturbed fields at the coupling surface. In the presence of active coils, two similar linear terms are added to the left hand side of Eq. (12), for the coil currents. Since the relation (12) is derived for all the poloidal harmonics of the solution field, the dimension of the vectors and matrices in (12) matches the number of total poloidal harmonics.

In the CarMa implementation, the relation (12) is computed by the eddy current code CARIDDI, assuming unit perturbations from the plasma. Then (12) is used as the boundary condition for MARS-F/K codes. Note that this is a linear boundary condition, which is very desirable if the MHD eigenvalue problem is also linear. The computational boundary for the MHD code now becomes the coupling surface. In principle, one can set the coupling surface directly at the plasma surface. We prefer a (narrow) vacuum gap between the plasma surface and the coupling surface for two reasons. First, we do not need to modify the plasma-vacuum interface conditions in MARS-F/K. Secondly, we avoid complications if there is a surface current generated at the plasma boundary due to the MHD perturbations.

The details of the backward coupling formulation are documented in Ref. [17]. This reference also reports the benchmark results for the CarMa implementation, as well as the first modelling results where all the important aspects of the RWM analysis - the rotation and kinetic effects, the 3D wall effects, the active control - are included in the same study. These results will not be shown in this paper.

3. Examples of recent results

3.1. Kinetic effects from fast ions

We show the fast ion effects on the RWM for a DIII-D plasma. Figure 1 shows the equilibrium profiles, reconstructed from the DIII-D discharge 125701 at 2.5s [33]. The $E \times B$ rotation profile corresponds to the critical profile measured in the experiment, when the RWM becomes marginally stable. The critical ω_E frequency is about 0.3% of the Alfvén frequency $\omega_A \equiv B_0/(R_0\sqrt{\mu_0\rho_0})$ at the $q = 2$ radial position, where ρ_0 is the plasma central density. The plasma major radius is $R_0 = 1.7$m. The toroidal

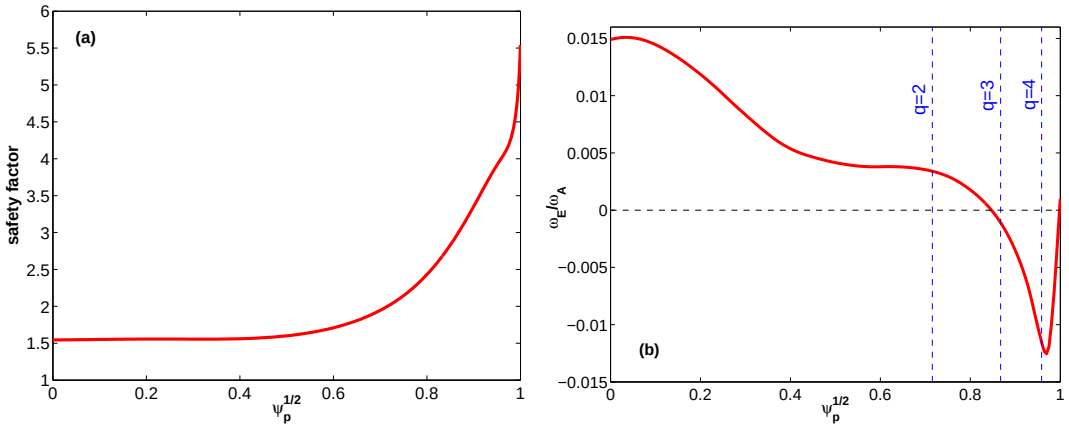

Figure 1. Equilibrium profiles, from the DIII-D discharge 125701 at 2.5s, used in the modelling, for (a) safety factor q, (b) plasma $E \times B$ toroidal rotation frequency normalised by the Alfvén frequency. ψ_p is the normalised poloidal magnetic flux.

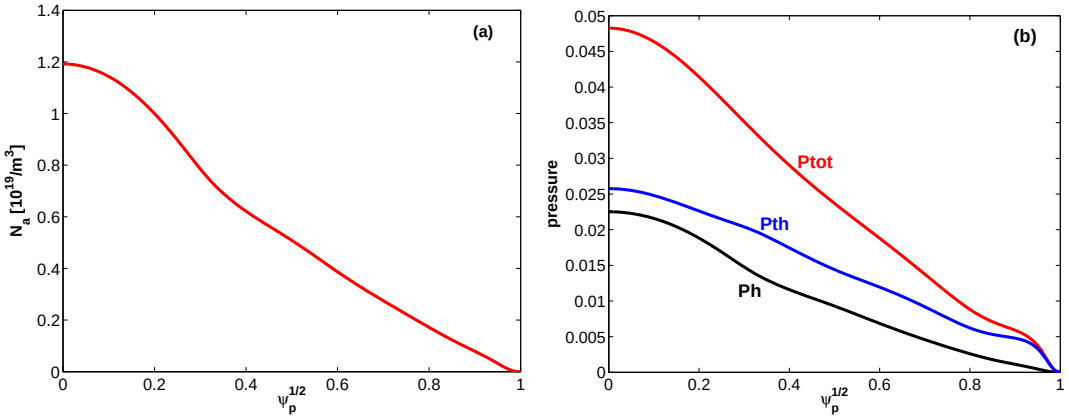

Figure 2. Experimental radial profiles of (a) the fast ion density and (b) the normalised pressure of fast and thermal ions.

magnetic field at the magnetic axis is $B_0 = 1.7$T. The total flat-top plasma current is $I_p = 1.14$MA for this discharge. Based on the same equilibrium, we have studied the kinetic effects of *thermal* particles on the RWM stability using MARS-K [34]. In this study, we compare the RWM stability with or without the *fast* ion kinetic effects. In both cases, we include kinetic contributions from toroidal precession drifts of trapped thermal ions and electrons. We fix the plasma pressure at the middle between the no-wall and ideal-wall beta limits for the ideal kink mode. This pressure is close to the experimental value. The DIII-D wall (vacuum vessel) shape is used, with a thin-wall assumption.

Figure 2 shows the experimental density and pressure profiles of the beam driven hot ions. The thermal and the total (thermal + hot ions) pressures are also plotted in Fig. 2(b). The pressures are normalised by the factor B_0^2/μ_0. For this DIII-D plasma, the beam driven fast ions contribute nearly half of the total plasma pressure.

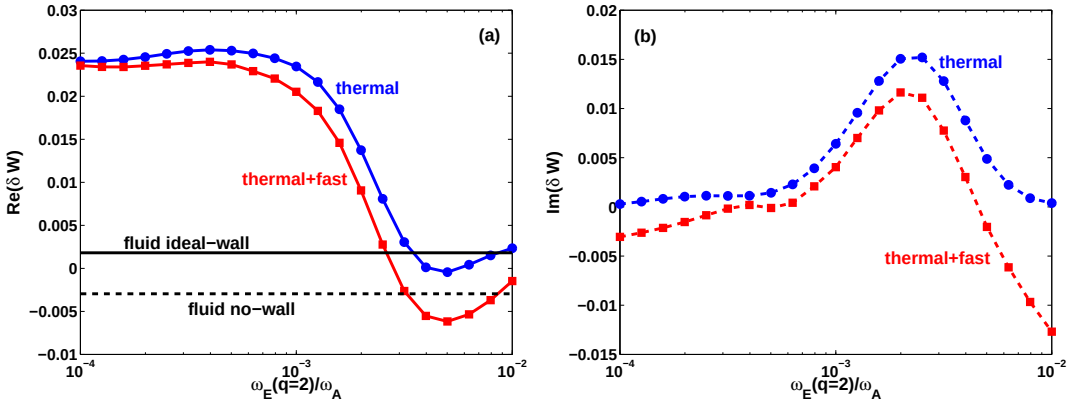

Figure 3. (a) Real and (b) imaginary part of the perturbed drift kinetic energy, computed by MARS-K following the perturbative approach. The total (ions + electrons) drift kinetic energy is compared with and without the fast ion contribution. The fluid potential energy with and without an ideal wall is also shown in (a).

We first show the results with the perturbative approach. Figure 3 compares the drift kinetic energy, with or without the fast ion contributions, versus the plasma $E \times B$ toroidal rotation frequency ω_E. We scale the rotation amplitude while fixing the rotation profile shown in Fig. 1(b).

In the perturbative calculations, the eigenfunction and the eigenvalue of the *static* fluid RWM (i.e. with vanishing plasma rotation) are used in evaluating the drift kinetic energy perturbation δW_k. At slow $E \times B$ rotation (below the experimental critical rotation frequency), the fast ions give minor contribution to δW_k. At faster rotation (ω_E close to 1% of ω_A at the $q = 2$ surface), the fast ions can give considerable contribution to δW_k, in particular for the imaginary part, which comes from the particle-wave resonances. This is expected, since a better match of frequencies occurs between the fast ion precession drifts and the RWM rotation (in the plasma frame) with increasing ω_E.

It is interesting to compare the amplitude of the drift kinetic energies to that of the fluid potential energies shown also in Fig.3(a). At slow ω_E, δW_k is significantly larger than δW_b or δW_∞. Hence the RWM stability would be determined predominantly by the drift kinetic effects, rather than the fluid effects. The real part of δW_k decreases at larger ω_E, but the finite imaginary part of δW_k still provides the stabilising effect to the mode.

Inserting the drift kinetic and the fluid energies from Fig.3 into the RWM dispersion relation (11), we obtain the mode eigenvalues shown in Fig.4. Figure 4(a) shows the growth/damping rate of the mode. Figure Fig.4(b) shows the real frequency of the mode in the laboratory frame.

At ω_E below or just above the experimental critical value, the perturbative approach predicts a full stabilisation of the RWM by the drift kinetic effects, with or without the fast ion contributions. The latter do not modify the mode damping rate nor the mode

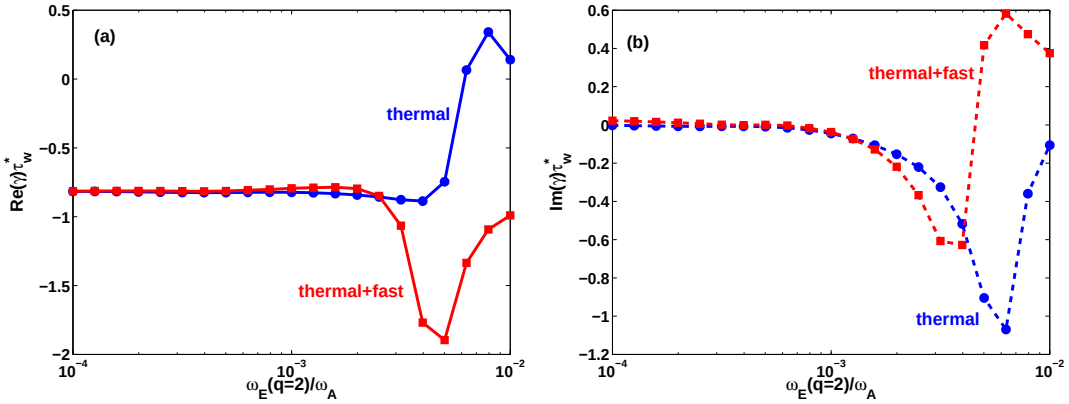

Figure 4. (a) Real and (b) imaginary part of the RWM eigenvalue, computed by MARS-K following the perturbative approach. The results with thermal particle kinetic effects, and with thermal and fast particle effects together, are compared.

frequency at slow $E \times B$ rotation, as compared with the case where only the thermal particle contributions are included.

At $\omega_E(q = 2)$ close to 1% of the Alfvén frequency, the thermal particle contributions alone seem to yield a narrow window of instability, whilst adding the fast ion contributions leads to a deeper stabilisation. Also, in this case the mode rotation switches direction with fast ions.

A rather different stability diagram is predicted by the self-consistent approach, as shown by Fig.5. Again we compare the mode eigenvalue versus the $E \times B$ rotation frequency with or without the fast ion contributions. With the thermal particle kinetic effects only, we observe two unstable branches: one at slow rotation, and one at fast rotation. These two branches sometimes leave a narrow stability window (depending on the plasma parameters such the pressure or density) [34], or sometimes nearly merge together as shown in this specific case. The unstable branch at small ω_E is completely different from that predicted by the perturbative approach. Within the eigenvalue approach, it is difficult to establish whether this branch represents a physical mode. Nevertheless, for two reasons investigated in detail in Ref. [34], the possibility of a numerical spurious solution seems to be excluded. One is the eigenmode structure for this branch, that resembles substantially the ordinary structure for a pressure-driven kink-ballooning RWM. Secondly, this unstable branch is also predicted by a simplified analytic model, proposed in [34].

With the inclusion of fast ions, the stability diagram (Fig. 5(a)) changes in three aspects. First, the fast ions *destabilise* the RWM in a wide range of ω_E ($0.002 < \omega_E(q = 2)/\omega_A < 0.007$), compared to the case with thermal particles alone. These destabilised modes, labelled here as the "fast-ion-driven" RWM, effectively close the stability window, that appears with the thermal particles. Secondly, as a result of the fast ion destabilisation and the roots merging, a second instability occurs, that has smaller growth rates and exists only in a finite window of ω_E. Thirdly, at sufficiently fast

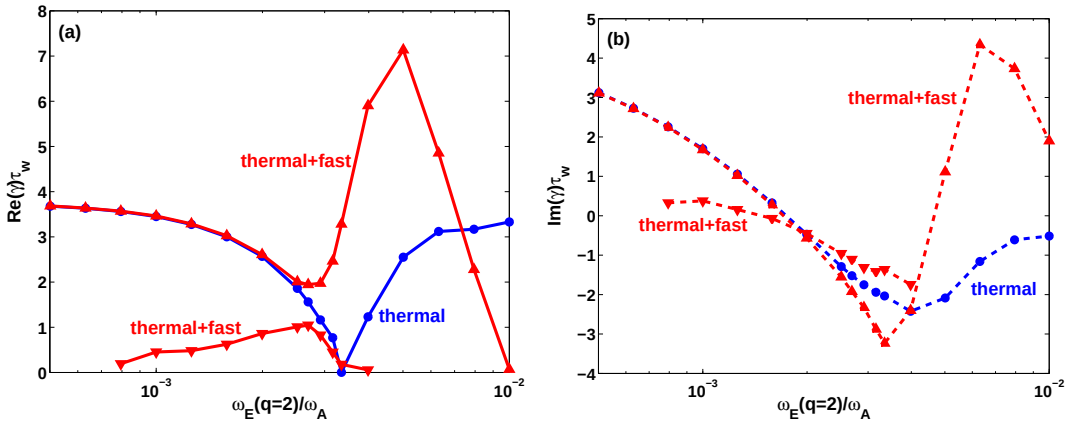

Figure 5. (a) Real and (b) imaginary part of the RWM eigenvalue, computed by MARS-K following the self-consistent approach. The results with thermal particle kinetic effects only (filled circles), and with thermal and fast particle effects together (filled triangles), are compared.

rotation ($\omega_E(q=2)/\omega_A > 1\%$ for this case), the self-consistent kinetic computations predict a full stabilisation of the RWM. This stabilisation is mainly due to the fast ions.

In the DIII-D experiment, the RWM seems to be stable for $\omega_E(q=2)/\omega_A > 0.3\%$ [33]. The discrepancy between the experiment and the self-consistent modelling requires further investigation. This can be due to the incompleteness of our drift kinetic model (e.g. lack of the finite orbit width effect and the thermal ion collisional effect, the crude approximation of the fast ions equilibrium distribution), or the presence of additional damping mechanism(s) in the experiment.

For the fast-ion-driven RWM, the mode frequency varies rapidly with increasing ω_E. The mode rotation can also change direction. However, the real frequency of the mode, in the laboratory frame, remains comparable to the inverse wall time.

Figure 6 compares the eigenmode structures for the two unstable modes at the experimental critical rotation frequency $\omega_E(q=2)/\omega_A = 0.3\%$. The poloidal Fourier harmonics of the normal displacement $\xi^1 \equiv \xi \cdot \nabla s$ are plotted, where s is the square root of the normalised poloidal flux. The two eigenfunctions are almost identical in the plasma core region. The differences appear beyond the $q=2$ rational surface. For the least unstable mode (dashed lines), a stronger singularity in the eigenmode structure is observed near the last rational surface $q=5$. The most pronounced differences in these two modes occur near the minor radius $s=0.95$.

We attribute two possible reasons to this observation. First, the trapped fast ions are mostly populated near the plasma edge region. Secondly, as shown in Fig.1(b), the $E \times B$ rotation profile has a second (negative) peak near $s=0.95$, making the rotation frequency ω_E comparable to the precession drift frequency of hot ions. This comparison is shown in Fig. 7, where the toroidal precession frequency ω_d^h of trapped hot ions is plotted as a function of the particle pitch angle Λ. The precession frequency is computed at the minor radius $s=0.95$, for the hot ions with the maximal particle kinetic energy

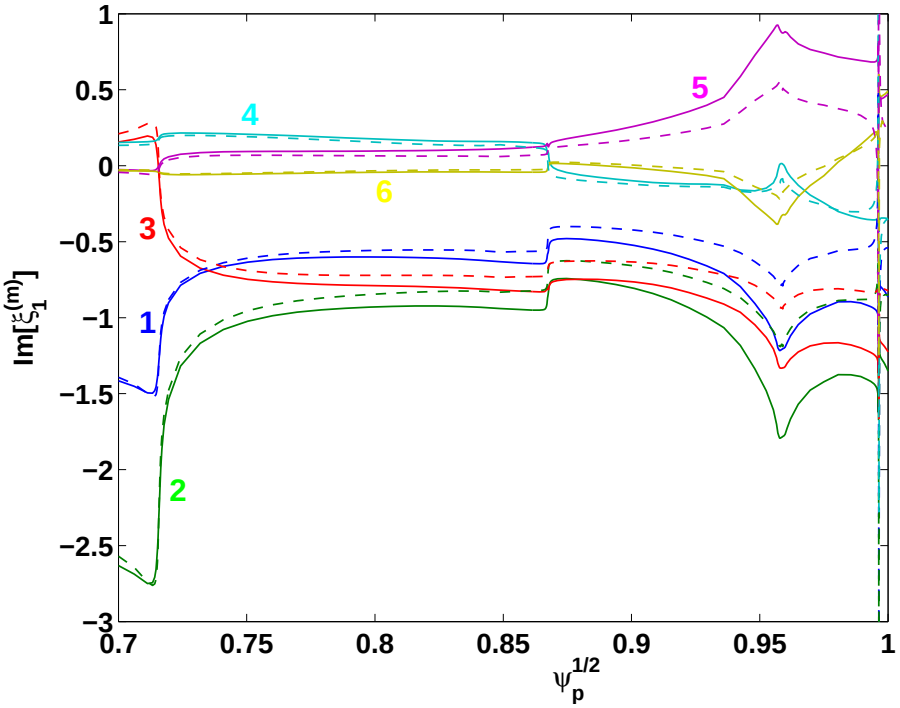

Figure 6. Comparison of the poloidal Fourier harmonics of the normal displacement in the equal-arc flux coordinate system, for the two branches of the kinetic RWM, with self-consistent inclusion of both thermal and fast particle kinetic effects. The eigenfunction shown by solid lines is more unstable than that by dashed lines. The eigenfunctions are similar in the plasma core region. The radial locations of the $q = 2, 3, 4, 5$ rational surfaces are $s \equiv \sqrt{\psi_p} = 0.7156, 0.8674, 0.9585, 0.9959$, respectively.

$\epsilon_k = \epsilon_{\max}$. The precession frequency of particles with less energy scales linearly with ϵ_k.

Adding the drift kinetic effects into the MHD equations brings in a new characteristic quantity associated specifically with the particle description (besides those fluid-related characteristic quantities such as the Alfvén time). Normally we choose this quantity as the ratio of the thermal ion gyro-frequency to the Alfvén frequency, ω_{ci}/ω_A, both defined at the magnetic axis. Since the precession frequency of both thermal and fast particles is inversely proportional to ω_{ci}/ω_A, we expect a sensitive dependence of the drift kinetic effects on this ratio. In practice, ω_{ci}/ω_A characterises various tokamak devices, since

$$\frac{\omega_{ci}}{\omega_A} = \frac{eR\sqrt{\mu_0 N}}{\sqrt{M}} \propto R\sqrt{N},$$

where M and N are the thermal ion's mass and mass density, respectively.

For the DIII-D plasma considered here, $\omega_{ci}/\omega_A = 27.3$, which was the value that we used for all the above results. For the self-consistent approach, we also made a sensitivity analysis of the kinetic effects against the variation of ω_{ci}/ω_A. The results are shown in Fig.8. We again obtain two branches of unstable kinetic RWM. One of them

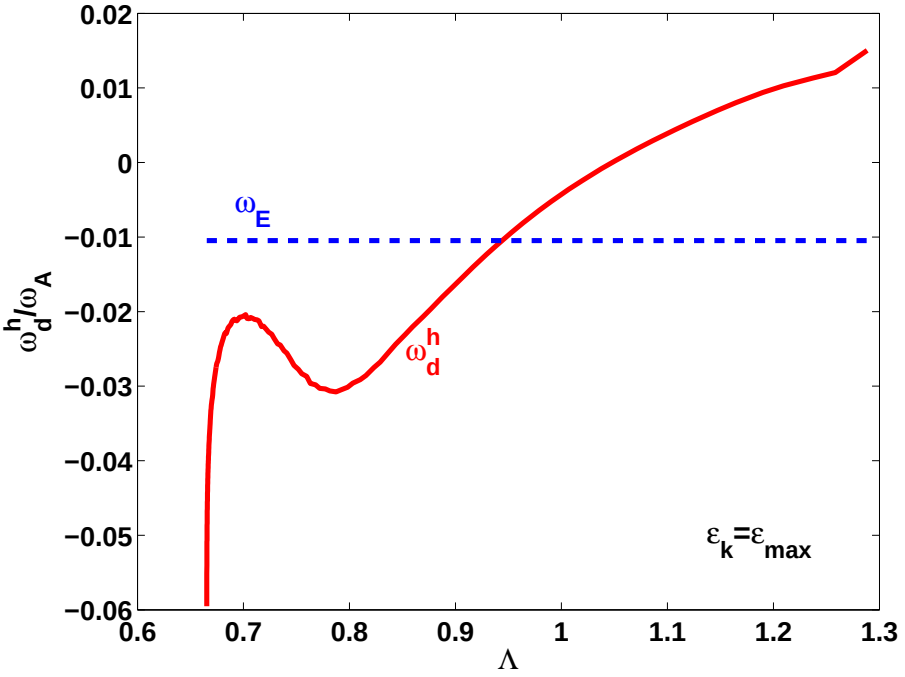

Figure 7. The precessional drift frequency of hot ions versus the pitch angle, at the maximal particle kinetic energy, compared with the plasma $E \times B$ toroidal rotation frequency. The comparison is made at the minor radius $s \equiv \sqrt{\psi_p} = 0.95$.

can be viewed as "driven" by fast ions at intermediate ω_{ci}/ω_A values and "stabilised" at large ω_{ci}/ω_A. The other one has a relatively narrow instability window. We notice that ω_{ci}/ω_A exceeds 100 for the ITER steady state plasmas. Hence this figure may indicate a stabilising effect of the fast ions on the RWM in ITER. However, a more rigorous prediction for ITER can only be made based on the self-consistent modelling for the ITER plasmas, whilst the computations shown here still assume the DIII-D equilibrium profiles, and the beam driven hot ions.

The qualitatively similar behaviour of the ω_{ci} scan to the ω_E scan as shown in Fig.5 is understandable. We note that these two parameters enter into the resonance operator for the drift kinetic energy as

$$\delta W_k \sim \frac{\omega_*}{\omega_E - C/\omega_{ci}},$$

where C is a constant related to the particle energy and the detailed orbit integration for the particle precession drift.

3.2. CarMa modelling for ITER

Extensive modelling of the RWM stability and control in ITER has been performed using the CarMa code [27, 28, 34, 24, 35, 30]. Below we give two examples of the recent results showing the capability of the code.

One of the key features of CarMa is the capability of solving large eddy current

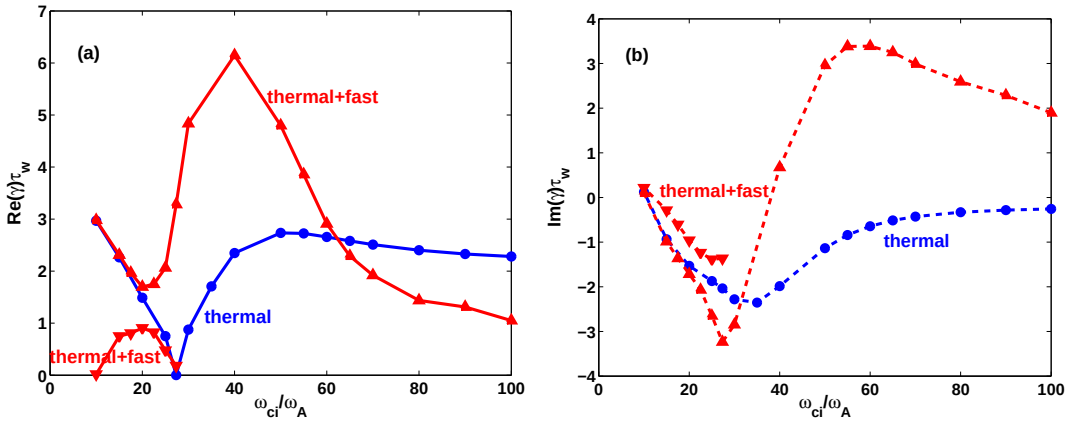

Figure 8. (a) Real and (b) imaginary part of the RWM eigenvalue, computed by MARS-K following the self-consistent approach. The thermal ion gyro-frequency is varied. The DIII-D plasma corresponds to $\omega_{ci}/\omega_A = 27.3$. The results with thermal particle kinetic effects only, and with thermal and fast particle effects together, are compared.

problems, resulting from complex geometry or sometimes volumetric discretisation of the conducting structures. Most of the RWM codes use the so-called Method of Moments to solve the eddy current problem, utilising the Green's function based integral formulations. This approach normally requires inverting a full system matrix, whose dimension is equal to the number of the degrees of freedom (DoF), associated with the eddy currents in conductors. Inversion of a large full matrix (say over 10000×10000) is computationally demanding. CarMa utilises an advanced fast technique [24], as well as parallel computing, allowing an eddy current problem with hundreds of thousands of DoFs to be solved.

Figure 9 shows a sector of the finite element mesh used in the CarMa computations for ITER. The double vacuum vessels are treated as thin shells. The thick blanket modules (BMs) are discretised using volumetric elements. Table 1 shows the influence of the blanket modules on the stability of the RWM in one of the ITER steady state plasmas. The results show that the inboard blanket modules do not significantly stabilise the mode. Most of the stabilising effect comes from the outboard BMs. This is expected because of the kink-ballooning nature of the low-n, pressure-driven RWM. The overall reduction of the RWM growth rate, due to the full set of BMs, is about 20% compared with the case without the BMs.

CarMa is also capable of performing multimodal analysis for the RWM stability and control [30]. For a realistic prediction of the operational space in ITER steady state plasmas, it is important to investigate the integrated effects of RWMs with different toroidal mode numbers. Shown in Fig. 10 is one particular example, where we study the mutual coupling between the $n = 0$ vertical stability and the $n = 1$ RWM. Without the feedback system (i.e. the open loop), the mutual coupling is caused by the 3D walls in ITER. A steady state plasma with $\beta_N = 2.7$ is chosen.

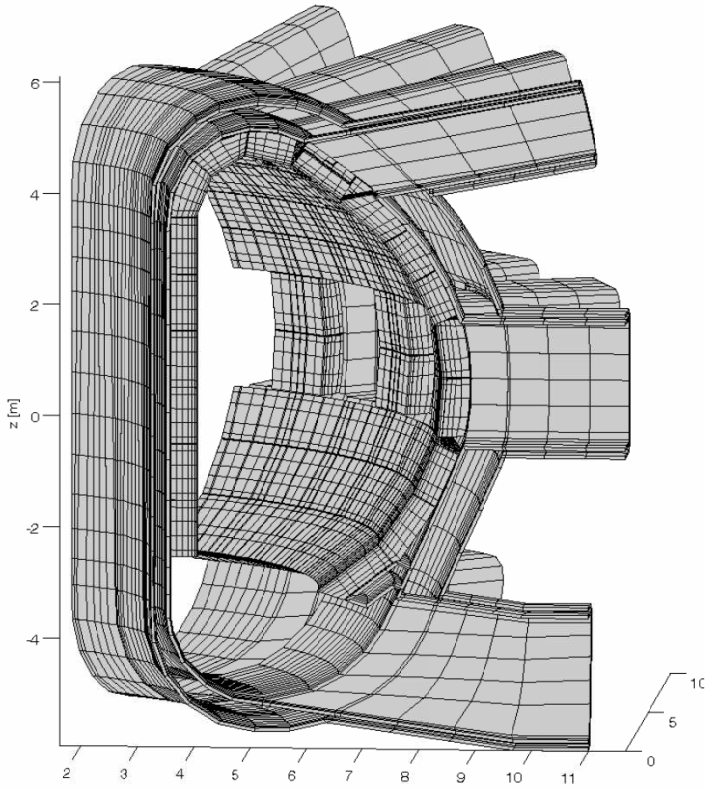

Figure 9. One toroidal segment of the finite element mesh used in the CarMa computations for ITER. The full mesh covers 360° toroidal angle. The volumetric elements are used to describe the blanket modules.

Table 1. CarMa computed growth rates of the $n = 1$ RWM in one of the ITER steady state plasmas, with 3D meshes for the vacuum vessels and the blanket modules (BM). The blanket modules are gradually added into the model.

BM rows included	# DoFs	growth rate γ [1/s]
None	24637	8.2
1-6 (inboard)	68485	8.2
14-18 (outboard)	89005	6.7
1-18 (all BMs)	206401	6.3

In the CarMa simulation, we choose an initial state where both the $n = 0$ and the $n = 1$ modes are present, with comparable amplitudes, and let these two modes evolve in time in the presence of 3D conducting structures. Figure 10 shows the eddy current patterns in the outer wall, after a suitable time interval. [The simulation time is long enough to allow the mode coupling to accur, but not until one of the modes becomes dominant whilst the other diminishes.]

Figure 10 shows a predominantly $n = 1$ eddy current pattern appearing near the outboard mid-plane, and a predominantly $n = 0$ pattern, that can be seen near the top of

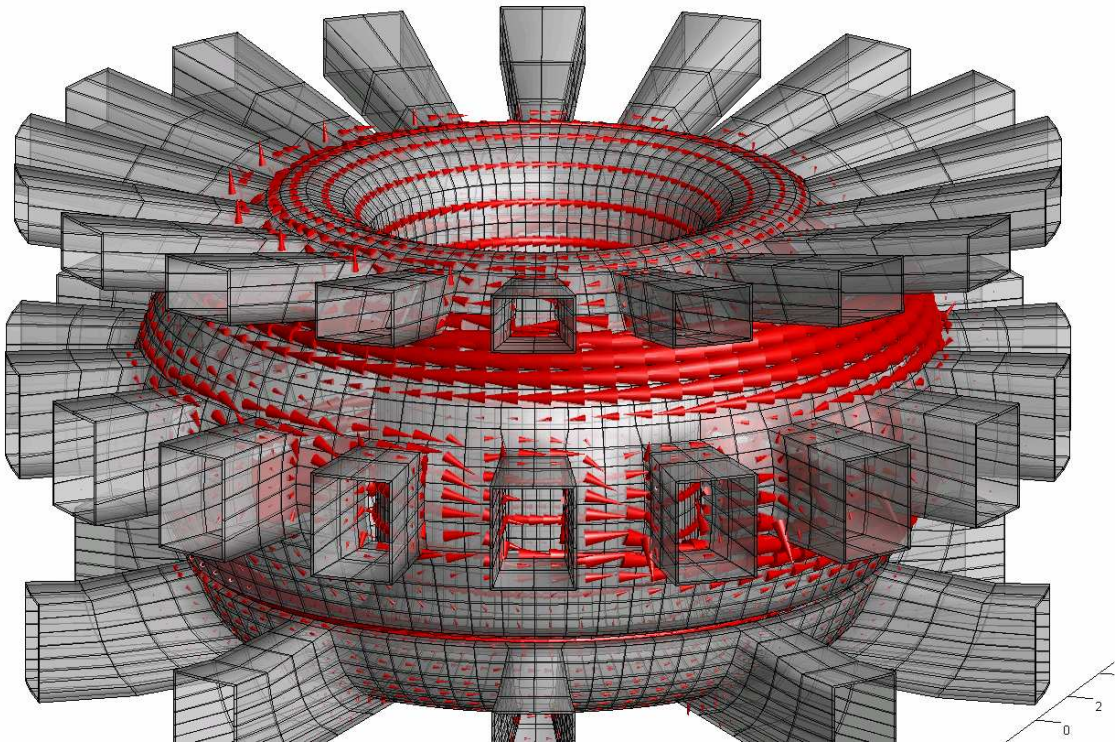

Figure 10. The wall eddy currents due to the simultaneously unstable $n = 0$ (vertical instability) and $n = 1$ (external kink) RWMs. Computations made by CarMa for the ITER steady state scenario at β_N=2.7.

the poloidal plane. These two patterns are well separated in this case, indicating a weak coupling between the $n = 0$ and the $n = 1$ modes. Indeed, the eigenvalue computations with CarMa find three eigenvalues $\gamma_1 = \gamma_2 = 10.4$ [1/s], and $\gamma_3 = 7.66$ [1/s]. The first two correspond to the predominantly $n = 1$ pattern, shifted by 90° toroidally. The third eigenvalue corresponds to the predominantly $n = 0$ pattern. These mode eigenvalues are almost identical to those found from monomodal computations.

3.3. Simulation of RWM feedback in RFX

With a realistic modelling of the 3D conducting structures in RFX, CarMa has been able to re-produce the measured open loop growth rates of the RWM with various toroidal mode numbers [29]. In the following, we report a comparison between the modelling and the experiment for the closed loop growth rates [35].

A toroidal RFP equilibrium is constructed by matching the so-called pinch parameter Θ and the reversal parameter F to the experimental values: $\Theta = 1.43, F = -0.06$. The equilibrium q-profile is shown in Fig.11. Since $q < q_0 = 0.152 < 1/6$, in the cylindrical approximation, the (internal) non-resonant modes (i.e. the RWM) are $n = -6, -5, -4, -3, ...$ with the poloidal mode number $m = 1$. For this equilibrium with shallow reversal, the most unstable mode, measured in the open loop experiment and predicted by the code, is the $n = -6$ mode. We carry out detailed closed loop

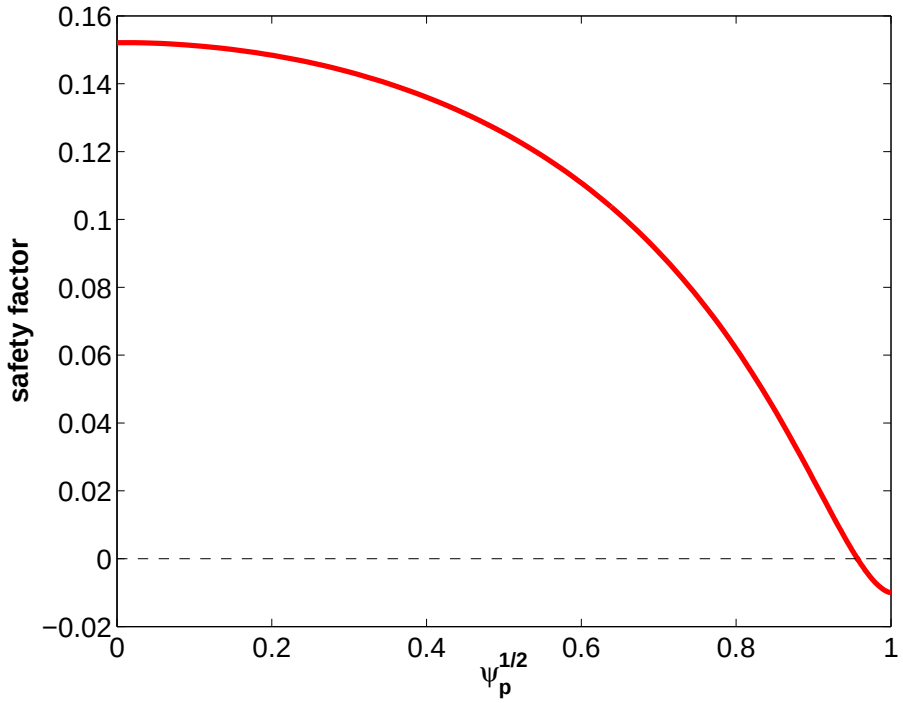

Figure 11. The profile of the safety factor for the RFX plasma with shallow field reversal: $\Theta = 1.43, F = -0.06$.

modelling for this mode, using the CarMa code.

The toroidicity couples all the poloidal harmonics and produces poloidal sidebands to the dominant $m = 1$ harmonic. [The aspect ratio for RFX is $R/a = 2[\mathrm{m}]/0.46[\mathrm{m}] = 4.35$.] In the CarMa analysis, we consider a single n number ($n = -6$), but include multiple poloidal harmonics.

Figure 12(a) shows the experimental time trace of the $m = 1, n = -6$ RWM amplitude, when a feedback with proportional gain is applied to the machine. These data allow extraction of the closed loop growth rates with a good accuracy [36]. On the other hand, the plasma response is also computed by the CarMa code. The CarMa model is then directly inserted into the same feedback loop, that is used in the experiment. The resulting "numerical" growth rates are compared with the experimental values in Fig.12(b), as a function of the feedback gain. Excellent agreement is obtained between the theory and the experiment, for both the closed loop growth rates, and the critical gain value needed for full suppression of the $n = -6$ mode.

4. Summary and discussion

The maturity of codes used to study the RWM is discussed. We consider both passive (plasma rotation, kinetic damping) and active (magnetic feedback) control of the RWM. As illustrative examples of the code development towards realistic modelling of RWM in the present and future fusion devices, we show the formulations and the computation

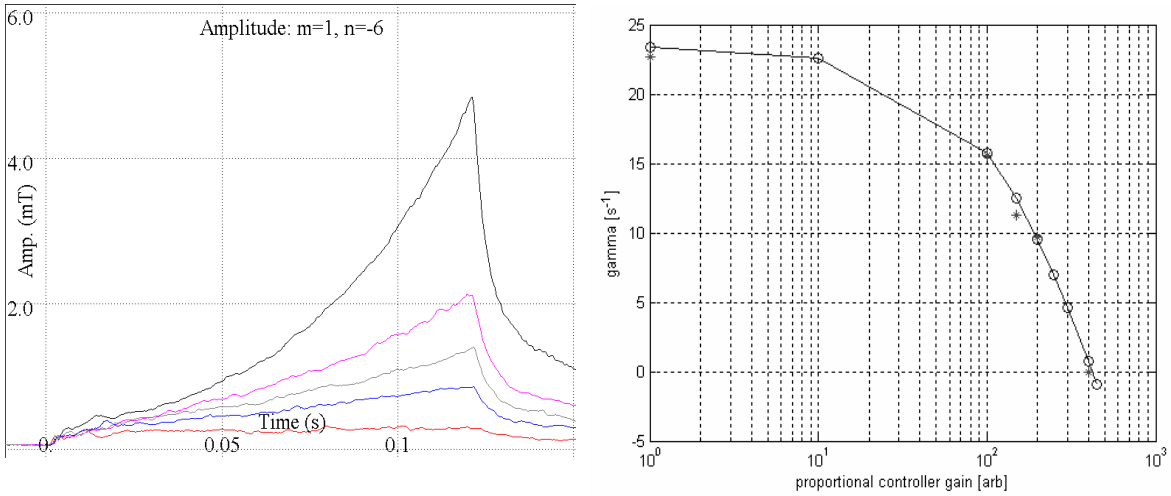

Figure 12. (a) The experimental data from the closed loop measurements. from which the closed loop growth rates of the $n = -6$ RWM are extracted. (b) Comparison of the closed loop growth rates from experiments ('*') and that from the CarMa modelling ('o'). In the latter case, the same feedback loop from the experiment is used, but with the plasma dynamics computed by the code.

results for the MARS-F/K code and the CarMa code.

Within a MHD-drift-kinetic hybrid model, the MARS-K results show that the self-consistent approach generally predicts less kinetic stabilisation on the RWM compared to perturbative approaches. The kinetic effects of the beam-driven hot ions on the RWM stability are modelled for a DIII-D equilibrium. The fast ion contributions, which can give additional stabilisation in the perturbative approach, also drives an extra unstable branch of mode in the self-consistent kinetic modelling.

The CarMa code allows a simultaneous modelling of 3D conductors, kinetic effects and feedback stabilisation for the RWM. The code is capable of performing large scale computations, where detailed 3D geometry of the conducting structures is included. The code is successfully applied to model the realistic feedback experiments in RFX.

We point out, however, that the current maturity status of the RWM codes still does not match the complexity of the RWM behaviour observed in tokamak experiments. In particular, no codes are available yet to study the non-linear coupling effects between the RWM and the other MHD modes observed in experiments. Some of the MHD-kinetic hybrid codes need a more complete inclusion of the drift kinetic effects. For example, the finite banana width (of fast ions), certain finite Lamour radius effects, and the (thermal ions) collision effects need to be included into MARS-K and some other codes. A better model of the equilibrium distribution function for the beam-driven hot ions should be considered.

The self-consistent kinetic modelling with MARS-K seems to predict a fast ion destabilisation of the RWM, in a certain plasma parameter space. Even though there seems to be experimental evidence on this possibility from other machines, no direct evidence is observed in DIII-D. Further investigations are needed in order to clarify

possible sources of the discrepancy between the modelling and the experiment.

Acknowledgments

This work was partly funded by the United Kingdom Engineering and Physical Sciences Research Council under grant EP/G003955 and the European Communities under the contract of Association between EURATOM and CCFE. The views and opinions expressed herein do not necessarily reflect those of the European Commission. Work also supported by the US Department of Energy under DE-FG03-956ER54309.

References

[1] Hender T C *et al* 2007 *Nucl. Fusion* **47** S128
[2] Chu M S and Okabayashi M 2009 *Plasma Phys. Control. Fusion* submitted
[3] Zheng L J *et al* 2008 *Proc. 22nd IAEA Fusion Energy Conf. 2008 (Geneva, Switzerland, 2008)* (Vienna: IAEA) TH/P9-32
[4] Lauber Ph *et al* 2007 *J. Comput. Phys.* **226** 447
[5] Hu B *et al* 2005 *Phys. Plasmas* **12** 057301
[6] Chapman I T *et al* 2009 *Plasma Phys. Control. Fusion* **51** 055015
[7] Liu Y Q *et al* 2008 *Phys. Plasmas* **15** 112503
[8] Bialek J *et al* 2001 *Phys. Plasmas* **8** 2170
[9] Merkel P *et al* 2006 *21st IAEA Fusion Energy Conf. 2006 (Chengdu, China)* (Vienna: IAEA) TH/P3-8
[10] Strumberger E *et al* 2008 *Phys. Plasmas* **15** 056110
[11] Albanese R *et al* 2008 *IEEE Trans. Magn.* **44** 1654
[12] Portone A *et al* 2008 *Plasma Phys. Control. Fusion* **50** 085004
[13] Liu Y Q *et al* 2000 *Phys. Plasmas* **7** 3681
[14] Chance M S *et al* 2002 *Nucl. Fusion* **42** 295
[15] Chu M S *et al* 2003 *Nucl. Fusion* **43** 441
[16] Degtyarev L *et al* 1997 *Comput. Phys. Comm.* **103** 10
[17] Liu Y Q and Villone F 2009 *Plasma Phys. Control. Fusion* **51** 115008
[18] Antonsen T M and Lee Y C 1982 *Phys. Fluids* **25** 132
[19] Porcelli F *et al* 1994 *Phys. Plasmas* **1** 470
[20] Haney S W and Freidberg J P 1989 *Phys. Fluids B* **1** 1637
[21] Chu M S *et al* 1995 *Phys. Plasmas* **2** 2236
[22] Albanese R and Rubinacci G 1998 *Advances in Imaging and Electron Physics* **102** 1
[23] Jin J M 1993 *The Finite Element Method in Electromagnetics* New York: John Wiley & Sons
[24] Rubinacci G *et al* 2009 *J. Comp. Phys.* **228** 1562
[25] Liu Y Q *et al* 2008 *Phys. Plasmas* **15** 072516
[26] Pustovitov V D 2008 *Plasma Phys. Control. Fusion* **50** 105001
[27] Villone F *et al* 2007 *Proc. 34th EPS Conference 2007 (Warsaw, Poland, 2007)* P5.125
[28] Villone F *et al* 2008 *Proc. 35th EPS Conference 2008 (Hersonissos, Greece, 2008)* P2.067
[29] Villone F *et al* 2008 *Phys. Rev. Lett.* **100** 255005
[30] Villone F *et al* 2009 *Proc. 36th EPS Conference 2009 (Sofia, Bulgaria, 2009)* P4.166
[31] Guazzotto L *et al* 2008 *Phys. Plasmas* **15** 072503
[32] Smith S P and Jardin S C 2008 *Phys. Plasmas* **15** 080701
[33] Reimerdes H *et al* 2007 *Phys. Rev. Lett.* **98**, 055001
[34] Liu Y Q *et al* 2009 *Phys. Plasmas* **16** 056113
[35] Villone F *et al* 2009 *Proc. 36th EPS Conference 2009 (Sofia, Bulgaria, 2009)* O4.028

[36] Baruzzo M *et al* 2009 *Proc. 36th EPS Conference 2009 (Sofia, Bulgaria, 2009)* P2.183